Ultrathin Fibers from Electrospinning Experiments under Driven Fast-Oscillating Perturbations

Ivan Coluzza,[1,2,*] Dario Pisignano,[3,4] Daniele Gentili,[1] Giuseppe Pontrelli,[1] and Sauro Succi[1]

[1]*CNR-Istituto per le Applicazioni del Calcolo "Mauro Picone," Via dei Taurini 19, I-00185 Rome, Italy*

[2]*Faculty of Physics, University of Vienna, Boltzmanngasse 5, 1090 Vienna, Austria*

[3]*Dipartimento di Matematica e Fisica "Ennio De Giorgi," Universita del Salento, via Arnesano, I-73100 Lecce, Italy*

[4]*National Nanotechnology Laboratory of Istituto Nanoscienze-CNR, via Arnesano, I-73100 Lecce, Italy*

(Received 7 May 2014; revised manuscript received 10 October 2014; published 19 November 2014)

The effects of a driven fast-oscillating spinneret on the bending instability of electrified jets, leading to the formation of spiral structures in electrospinning experiments with charged polymers, are explored by means of extensive computer simulations. It is found that the morphology of the spirals can be placed in direct correspondence with the oscillation frequency and amplitude. In particular, by increasing the oscillation amplitude and frequency, thinner fibers can be extracted by the same polymer material, thereby opening design scenarios in electrospinning experiments.

DOI: 10.1103/PhysRevApplied.2.054011

I. INTRODUCTION

The dynamics of charged polymer jets under the effect of an external electrostatic field stands out as a major challenge in nonequilibrium thermodynamics, with numerous applications in micro- and nanoengineering and life sciences as well [1–11]. Indeed, charged liquid jets may develop several types of instabilities depending on the relative strength of the various forces acting upon them, primarily electrostatic Coulomb self-repulsion, viscoelastic drag, and surface tension effects. Among others, one should mention bending and "whipping" instabilities, the latter consisting of fast large-scale lashes, resembling the action of a whip. These instabilities are central to the manufacturing process known as electrospinning [12–17]. Some of them were analyzed in the late 1960s by Taylor [18]. In the subsequent years, it became clear that the driver of such instabilities is the Coulomb self-repulsion, as can be inferred by simply observing that any off-axis perturbation of a collinear set of equal-sign charges would only grow under the effect of Coulomb repulsion [2,19].

In the electrospinning process, ultrathin fibers, with diameters in the range of hundreds of nanometers and below, are produced out of charged polymer jets. In addition to its fundamental importance in the fields of soft matter physics and fluid dynamics, electrospinning is raising a continuously increasing interest due to its widespread application fields. For this reason, nowadays this technique is an excellent example of how applied physics impacts on engineering and materials science. For example, recently, electrospun nanofibers and nanowires have been used for realizing organic field-effect transistors [11,20], whose fabrication benefits from the concomitant high spatial resolution of active channels, large-area deposition, and frequently improved charge-carrier mobility, which is highly relevant for nanoelectronics. Other important applications are in the field of photonics [16] and include solid-state organic lasers [21], light-emitting devices [22,23], and active nanomaterials featuring high internal orientational order of embedded chromophores, thus exhibiting polarized infrared, Raman [24–26], and emission spectra [27]. Electrohydrodynamics jet printing has been recently applied in order to control the hierarchical self-assembly of patterns in deposited block-copolymer films [10], with important applications in nanomanufacturing and surface engineering. Electrostatic spinning is also a tool for medical sciences and regenerative medicine, e.g., for the construction of complex scaffolding necessary for tissue growth [8,28] or for the accurate encapsulation of solutions into monodisperse drops [4]. In general, electrospinning is an excellent technique to transfer to a macroscopic composite material the properties of complex polymer solutions [5], which can have a direct impact on the mechanical properties of resulting nanofibers [29]. In this respect, an aspect which is particularly critical is that fibers can reach a diameter in the nanometer scale. Electrospinning can reach such scales, especially thanks to the occurrence of instabilities that drive the system to extend on the plane orthogonal to the jet axis [1–3,6,7,9]. In such experiments, a droplet of charged polymer solution is injected from a nozzle at one end of the apparatus (spinneret); then it is elongated, and the resulting collinear jet moves away from the droplet under the effect of an externally applied electrostatic field. Such a collinear configuration is, however, unstable against off-axis perturbations, as one can readily realize by inspecting the effect of Coulomb

*i.coluzza@iac.cnr.it;ivan.coluzza@univie.ac.at

repulsion on different portions of the jet. The resulting bending instability often gives rise to three-dimensional helicoidal structures (spirals). Because of polymer mass conservation, the spiral structures get thinner and thinner as they proceed downwards, until they hit a collecting plate at the bottom. Based on the above, it is clear that an accurate control of the effects of the bending and whipping instabilities on the morphological features of the resulting spirals is key to an efficient design of the electrospinning process. The fundamental physics of the electrospinning process is governed by the competition between Coulomb repulsion and the stabilizing effects of viscoelastic drag and surface tension. Since the time span of the entire process is comparable with the relaxation time of the polymer material, electrospinning qualifies as a strongly off-equilibrium process.

A number of papers deal with the theory of the electrospinning process [1,2,15,30–33]. Broadly speaking, these models fall within two general classes: continuum and discrete. The former treat the polymer jet as a charged fluid, obeying the equations of continuum mechanics, while the latter represent the jet as a discrete collection of charged particles (beads), subject to four type of interactions: Coulomb repulsion, viscoelastic drag, curvature-driven surface tension, and, finally, the external electric field.

However, due to the complexity of the resulting dynamics and to the large number of experimental parameters involved in the process (related to solution, field, and environmental properties), electrified jets are still treated by empirical approaches. For instance, either near-field techniques have been proposed to reduce instabilities [34,35], or the effects of the different parameters on the resulting nanofiber properties and radius have been determined empirically through systematic campaigns [7,36]. Indeed, to date, most investigations on electrospinning focus on the experimental exploration of the various types of polymers that are liable to be electrospun into fibers, as well as on the processing and properties of the spun fibers.

In addition, the dynamics of the jet is also sensitive to random external disturbances (noise) and particularly to erratic oscillations of the injection apparatus and of ambient atmosphere, which could act as hidden variables critically affecting the reliability of the process. In the following, we shall consider such fast mechanical oscillations of the spinneret as a driving perturbation, whose amplitude and frequency can be fine-tuned in order to minimize the thickness of the electrospun fiber. This approach portrays an angle of investigation of the electrospinning process that we proceed to investigate, on a systematic basis in this paper. In particular, it is found that increasing either the perturbation amplitude, frequency, or both can lead to obtaining thinner jets, hence thinner fibers in the end. More precisely, by increasing the perturbation amplitude, spirals are seen to open up into a broader cone envelope, hence resulting in thinner fibers. By increasing the perturbation frequency, on the other hand, the spirals are developed with a shorter pitch, resulting again in thinner fibers at the collecting plate. To highlight the potential of driving the injected fluid to produce thinner fibers in practice, we point out that increasing the perturbation amplitudes, from, say, 1.6×10^{-4} to 1.6×10^{-3} cm, while keeping the other process parameters unchanged, leads to a threefold reduction of the resulting fiber thickness for polyethylene oxide and other plastic materials. Similarly, varying the perturbation frequency from 10^5 to 10^6 s^{-1} determines a threefold fiber thickness decrease.

II. MATHEMATICAL MODEL

The mathematical model used in this paper closely follows the one given in the pioneering work by Reneker and co-workers [2]; namely, the jet is described by a sequence of discrete charged particles (beads), obeying Maxwell fluid mechanics under the effects of the four forces described above. The polymer jet is represented by means of a Maxwellian liquid, coarse-grained into a viscoelastic bead-spring model with a charge associated to each bead. This representation is justified by the earlier work of Yarin [1,37]. In Fig. 1, we show what the experimental setup looks like. On the top of the figure, there is the pendant drop, which is dangling from a pipette or from a syringe. Between the pipette placed along the Z axis at a height h and the collecting plane (not visible in the figure) at $Z = 0$, the electric field V_0/h is applied downwards along the Z direction. We shall consider the following experimental parameters: a_0 is the initial cross-section radius of the electrified jet, e is the charge per particle, G is the elastic modulus, h is the distance from the

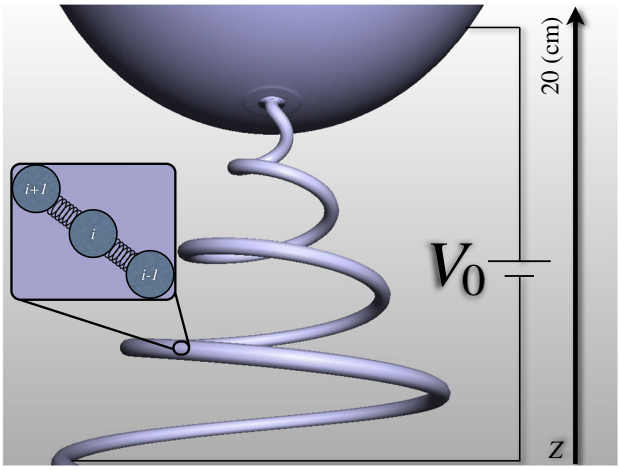

FIG. 1. Schematic representation of the model for the polymer jet. The jet is generated from the pendant drop on the top of the figure upon application of the external field V_0/h. The jet is then represented at a microscopic level as a bead-spring chain. Each bead is charged while the connecting springs are calculated by solving the associated polymer stress equations at each molecular dynamics time step.

drop to the collector, m is the mass of each particle, μ is the dynamic viscosity, $\theta = \mu/G$ is the relaxation time, α is the surface tension, and V_0 is the voltage applied between the drop and the grounded collector plate. In what follows, we will use Gaussian units for charges (CGS units). In Fig. 1, the spring represents the stress σ in the Maxwellian fluid, and it is determined by the stress equation between each consecutive pair of beads. The coupled system of Newton equations for the beads and the associated stress equation reads as follows:

$$m\frac{d^2\vec{R}_i}{dt^2} = \vec{F}_i, \qquad \frac{d\sigma_i}{dt} = \frac{1}{l_i}\frac{dl_i}{dt} - \sigma_i, \tag{1}$$

where $\vec{R}_i = (X_i, Y_i, Z_i)$ is the position vector of the ith bead and $l_i = [\Delta X_i{}^2 + \Delta Y_i{}^2 + \Delta Z_i{}^2]^{1/2}$ is the distance between two bonded beads. Space and time units are chosen as $t = t_{\rm phys}/\theta$ and $l = l_{\rm phys}/L$, where $L = (e^2/\pi a_0^2 G)^{1/2}$. In the following, the superscript (subscript) U (respectively, D) will refer to the "up" $(i+1)$ and "down" $(i-1)$ beads, respectively, where i is the bead index. The coupling between the equations in Eq. (1) takes place through the net viscoelastic force $\vec{F}_{\rm VE}$ acting on the bead i, which is given by

$$\begin{aligned}\vec{F}_{\rm VE} = F_{\rm ve}\Bigg[&\left(a_U^2\sigma_i^U\frac{X_{i+1}-X_i}{l_i^U} - a_D^2\sigma_i^D\frac{X_i - X_{i-1}}{l_i^D}\right)\vec{i}\\ &+\left(a_U^2\sigma_i^U\frac{Y_{i+1}-Y_i}{l_i^U} - a_D^2\sigma_i^D\frac{Y_i - Y_{i-1}}{l_i^D}\right)\vec{j}\\ &+\left(a_U^2\sigma_i^U\frac{Z_{i+1}-Z_i}{l_i^U} - a_D^2\sigma_i^D\frac{Z_i - Z_{i-1}}{l_i^D}\right)\vec{k}\Bigg],\end{aligned} \tag{2}$$

where in reduced units one has $a_U^2 = 1/l_i^U$ and $a_D^2 = 1/l_i^D$. Besides the viscoelastic force $\vec{F}_{\rm VE}$, each bead is subject to three additional forces: namely, the driving force $\vec{F}_0$ of the external field $\vec{V}_0$, acting between the drop and the collection plate, the bead-bead Coulomb interaction $\vec{F}_{\rm Coul}$, and the surface tension force $\vec{F}_{\rm cap}$, which acts as an effective bending rigidity penalizing curved jet shapes. These forces read as follows:

$$\begin{aligned}\vec{F}_0 &= -\frac{e\mu^2|\vec{V}_0|}{hLmG^2}\vec{k},\\ \vec{F}_{\rm Coul} &= Q\sum_j\left(\frac{X_i - X_j}{R_{ij}^3}\vec{i} + \frac{Y_i - Y_j}{R_{ij}^3}\vec{j} + \frac{Z_i - z_j}{R_{ij}^3}\vec{k}\right),\\ \vec{F}_{\rm cap} &= Ak_i\left(-X_i\frac{(a_U + a_D)^2}{4\sqrt{X_i^2 + Y_i^2}}\vec{i} - Y_i\frac{(a_U + a_D)^2}{4\sqrt{X_i^2 + Y_i^2}}\vec{j}\right),\end{aligned} \tag{3}$$

where $F_{\rm ve} \equiv Q = \frac{\pi a_0^2\mu^2}{LmG}$, $A = \frac{\pi\alpha a_0^2\mu^2}{mL^2G^2}$, R_{ij} is the distance between two beads, and k_i is the local curvature, defined as the radius of the circle going through the points $i+1$, i, and $i-1$. It is important to stress that the model also assumes that the fluid is incompressible, which results in the mass conservation law:

$$\pi a^2 l = \pi a_0^2 l_0. \tag{4}$$

This determines the fiber thickness a as a function of the elongation l. At each time step, we first integrate the above stress equations in Eq. (1), and then we use the updated stress terms to integrate the equations of motion which, in turn, are solved with a simple velocity Verlet integration scheme with the same integration time step Δt used for the stress equation.

III. NUMERICAL INTEGRATION SCHEME

We solve Eq. (1) in an equivalent but numerically more convenient form:

$$\frac{d(e^t\sigma)}{dt} = e^t\left(\frac{1}{l}\frac{dl}{dt}\right) \tag{5}$$

by using the forward Euler discrete integration scheme with an integration step Δt:

$$e^t\sigma(t) - e^{t-\Delta t}\sigma(t-\Delta t) = \Delta t e^t\left(\frac{1}{l(t)}\frac{l(t) - l(t-\Delta t)}{\Delta t}\right), \tag{6}$$

which leads to the explicit time-marching scheme

$$\sigma(t) = e^{-\Delta t}\sigma(t-\Delta t) + \frac{l(t) - l(t-\Delta t)}{l(t)}. \tag{7}$$

The Euler integration is coupled to a Verlet time integration scheme as follows, given the initial conditions at $t = -\Delta t$ and at $t = 0$:

(1) Stress at time t: $\sigma(t-\Delta t) \to \sigma(t)$ from Eq. (7).
(2) Forces at time t: $\vec{F}(t) = \vec{F}_{\rm VE} + \vec{F}_{\rm Coul} + \vec{F}_{\rm cap} + \vec{F}_0$.
(3) Positions at time $t+\Delta t$: $\vec{r}(t+\Delta t) = 2\vec{r}(t) - \vec{r}(t-\Delta t) + \vec{F}(t)\Delta t^2$.
(4) Velocities at time $t+\Delta t$: $\vec{v}(t+\Delta t) = [\vec{r}(t+\Delta t) - \vec{r}(t-\Delta t)]/(2\Delta t)$.

We point out that the $1/r^2$ Coulomb singularity needs to be handled with great care, especially at the injection stage, where beads are inserted at a mutual distance shorter than their linear size. This care imposes very small time steps, of the order of 10^{-8} μ/G.

The effect of mechanical oscillations is mimicked by injecting the tail bead $i = N(t)$; $\vec{V}_{\rm init}^{\,i} = 0$, $N(t)$ being the number of beads in the chain at time t, at an off-axis position given by

$$X_N = N_s L\cos(\Omega t), \tag{8}$$

$$Y_N = N_s L \sin(\Omega t), \tag{9}$$

$$Z_N = h - L_{\text{ins}}, \tag{10}$$

where $L_{\text{ins}} = h/I_F$ is the insertion length and I_F the insertion factor, h is the vertical size of the apparatus, typically $I_F = 50\,000$, $N_s \ll 1$ is the amplitude, and Ω is the frequency of the dynamical perturbation. In the following, we shall refer to N_s as the noise strength. We remind the reader that the insertion algorithm proceeds by inserting the Nth bead (polymer jet tail) once the distance between the $(N-1)$th bead and the pendant drop at $Z = h$ exceeds the insertion distance $L_{\text{ins}} = h/I_F$. Thus, the jet is represented by a bead chain with the tail, $i = N$, at the spinneret and the head, $i = 1$, proceeding downwards to the collector. The idea behind this model [2] is that, by choosing $\Omega \gg 1$, the above algorithm will generate a quasirandom sequence of initial slopes of the polymer bead chain, whose envelope defines a conical surface known as the Taylor cone. In this work, however, the expression (8) and (9) stands for a deterministic, *controlled* source of fast oscillations, whose amplitude and frequencies can be fine-tuned to design thinner fibers. To quantitatively explore this idea, we run simulations with several values of the perturbation strength N_s and perturbation frequency Ω.

Boundary conditions are imposed at the two ends of the jet: at $Z = h$ (top) and at the collecting plate $Z = 0$ (bottom). The latter is treated as an impenetrable plane, at which the Coulomb forces are set to zero and the Z component of the bead position is not allowed to take negative values. The top boundary condition is such that the X and Y components of the forces acting on the pendant drop are set to zero, while the Z component must be nonpositive, i.e., point downwards.

In what follows, we use the scheme above to solve the time development of the jet with a reference set of parameters pretty close, yet not exactly equal to the one given in the original paper by Reneker *et al.* [2] as presented in Table I. For the case in point, $L = 0.32$ cm and $\theta = 0.01$ s. The resulting dimensionless parameters are given in the right panel of Table I, where Q, F_{ve}, and A are the strength of the Coulomb repulsion, viscoelastic forces, and surface tension, respectively, $K_s = \Omega\theta$ is the injection frequency, $H = h/L$, and $\vec{F}_0$ is the scaled force resulting from the external field, all in dimensionless units.

TABLE I. Simulation parameters obtained from the experimental data in the paper of Reneker *et al.* [2].

Experimental parameters	Simulation parameters
$\alpha = 700$ g/s^2	
$a_0 = 1.5 \times 10^{-2}$ cm	
$e = 8.48$ $\frac{\text{g}^{1/2}\,\text{cm}^{3/2}}{\text{s}}$	
$\theta = 0.01$ s	$Q \equiv F_{\text{ve}} = 78309.8$ [Eq. (3)]
$G = 10^6$ $\frac{\text{g}}{\text{cm s}^2}$	$F_0 = 157.9$ [Eq. (3)]
$h = 20$ cm	$A = 171.9$ [Eq. (3)]
$m = 2.83 \times 10^{-6}$ g	$K_s = 100$
$\mu = 10^4$ $\frac{\text{g}}{\text{cm s}}$	$H = 62.8$
$V_0 = 10^4$ V	
$\Omega = 10^4$ s^{-1}	

IV. RESULTS AND DISCUSSION

In Fig. 2(a), we show a typical shape of the jet at the end of a simulation, lasting about 10^6 time steps. As one can appreciate, spirals show from three to about ten turns over distances of a few centimeters, which is consistent with experimental observation [38,39]. While we cannot rule out the possibility that kinematic effects play a major role in the spiral formation, we must observe that the morphology of the spiral appears highly dependent on the choice of the initial conditions and forcing parameters. In this respect, even the kinematics alone may not be trivial at all. We also consider a scenario whereby the perturbation is not applied on the XY plane, but only along the X axis. Since the component of the force along the Y axis is always zero, the jet does not develop any component in the YZ plane, resulting in a flat sinusoidal profile in the XZ plane [Fig. 2(b)]. Also, these classes of planar spirals are frequently observed in experiments and not explored in previous theoretical papers. The extreme variability of experimentally observed spirals can therefore be accounted for by considering the oscillating perturbation as an independent variable affecting the resulting dynamics of the electrified jets.

A. Effect of the perturbation amplitude

One of the environmental parameters of the model is the amplitude of the noise on the pendant drop, related to the

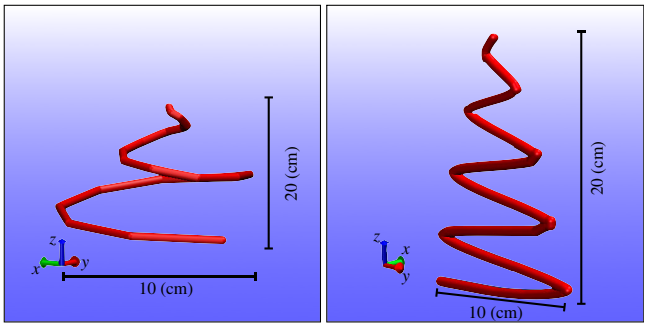

(a) (b)

FIG. 2. Final configuration of the filament in the case of a circular driving perturbation (a) and a linear one (b). Parameters used for the simulations are $V_0 = 10^4$ V, $\Omega = 5 \times 10^5$ s^{-1}, $N_s = 10^{-3}$, and the total spinneret-collector distance $h = 20$ cm, which results in the rescaled quantities $L = 0.32$, $Q = F_{\text{ve}} = 78\,309.8$, $F_0 = 157.9$, $A = 171.9$, and $H = 62.8$. The linear dimensions are depicted in the figure and correspond to the following range of the axes: $X \in [-5, 5]$ cm, $Y \in [-5, 5]$ cm, and $Z \in [0, 20]$ cm.

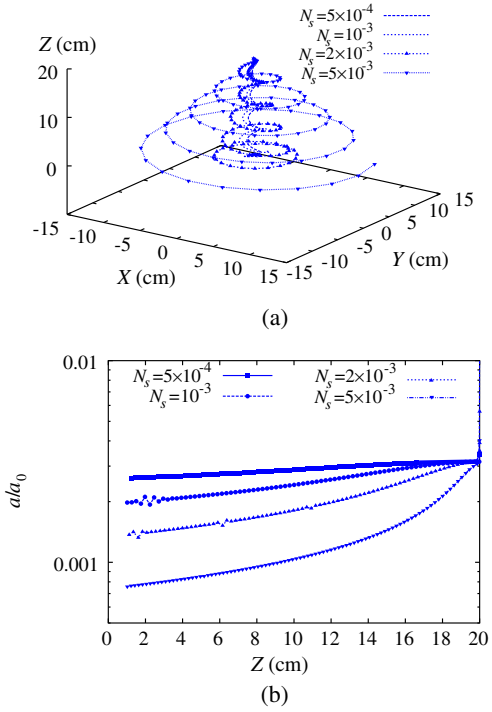

FIG. 3. Effect on the spiral shape of the mechanical perturbation applied to the pendant drop. (a) Final configuration. Parameters used for the simulations are as above except for N_s. The plot shows the comparison of the profiles obtained with different values of the perturbation strength N_s. (b) Plot of the elongation along the spiral as a function of the distance from the collector. The plot shows a monotonic decrease of the fiber thickness as a function of the distance from the pendant drop. Finally, the plot highlights that an increase in the spiral radius induces an increase in the elongation of the electrified jet and correspondingly a reduction of the diameter of the resulting fibers.

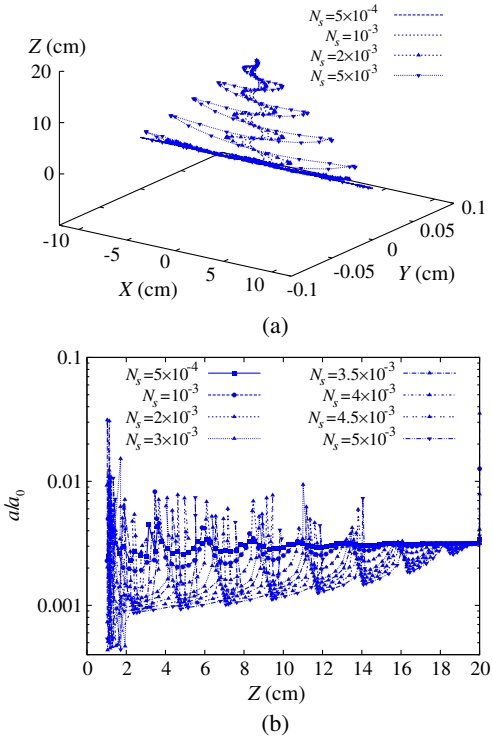

FIG. 4. Effect on the spiral shape of the perturbation applied to the pendant drop only along the X axis. (a) Final configuration of the filament. Parameters used for the simulations are $V_0 = 10^4$ V, $\Omega = 5 \times 10^5$ s^{-1}, and $h = 20$ cm. The plot compares the profiles obtained with different values of the noise strength N_s, with the jet oscillating only in the XZ plane. (b) Plot of the elongation as a function of the distance from the collector. The spikes, not present in the case of the circular applied perturbation, correspond to the bending points that occur along the Z axis.

vibrations that affect the experiment at the microscale. In the paper of Reneker *et al.* [2], the noise amplitude is kept fixed to $N_s = 10^{-3}$. In Fig. 3, we show the comparison between the results in the amplitude range $N_s \in [5 \times 10^{-4}, \ldots, 5 \times 10^{-3}]$. The main effect of increasing the amplitude is to increase the aperture of the spiral, basically in linear proportion. This increase indicates that the spiral keeps full memory of its initial slope, which is consistent with the deterministic nature of the model.

In Fig. 3(b), we show the running draw ratio $a(Z)/a_0$ along the polymer chain, consisting of about 100 discrete beads, for different values of the noise strength N_s. The final draw ratio is computed according to the standard expression resulting from mass conservation between the head (index 0) and tail (index f) dimers in the chain, namely, $\frac{a_f}{a_0} = \sqrt{\frac{cL_{\text{ins}}}{l_{\text{final}}}}$, where $c = 0.06$ is the initial polymer concentration in the solution and l_{final} is the elongation of the bead closer to the collecting plane at end of the simulation. As expected by mass conservation, at all values of N_s, the jet thickness is a decreasing function of the distance from the spinneret ($Z = 20$). Such a decreasing trend is more and more pronounced as N_s is increased. For the bead closest to the collector, the draw ratio goes from $a_f/a_0 = 2.5 \times 10^{-3}$ for $N_s = 5 \times 10^{-4}$ to about $a_f/a_0 = 7.5 \times 10^{-4}$ for $N_s = 5 \times 10^{-3}$. Thus, an order of magnitude increase in the perturbation amplitude leads to a factor-3 reduction in the fiber thickness.

By inspecting the extension of the jet, it is seen that, on average, the thickness is still reduced by a similar amount as in the case of the planar perturbation (Fig. 4). However, at variance with the case of planar perturbation, the elongation shows recurrent oscillations, due to the fact that, close to the turning points, the fiber gets compressed, resulting in a local increase of its thickness. Such a compression, which is visible in Fig. 2(b) through the blobs at the turning points, is a purely two-dimensional effect, since in three dimensions the bead can turn back by taking a *smooth* round trip around the Z axis. This two-dimensional topological constraint leads to the peculiar bananalike shape of the oscillation at high values of the perturbation amplitude, $N_s = 5 \times 10^{-3}$ [Fig. 4(a)], which

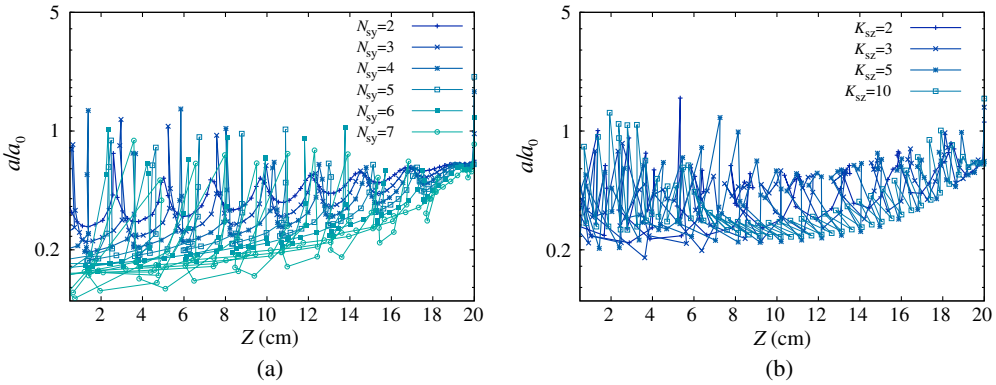

FIG. 5. Plot of the fiber thickness a/a_0 as a function of the height from the collecting plane at $Z = 0$. We considered both asymmetric planar noises (X/Y noise ratio $N_{\mathrm{sy}} > 1$) and vertical noises along the Z axis (XY/Z relative noise amplitude $N_{sz} = 1$ and relative frequency $K_{sz} > 1$). Parameters used for the simulations are $V_0 = 10^4$ V, $I_F = 5 \times 10^4$, $N_s = 10^{-3}$, and $h = 20$ cm. As for the 1D noise scenario, the elongation profile strongly fluctuates with the height from the collecting plate, making asymmetric or vertical driving forces not desirable for optimal experimental setup.

results in large spikes of the fiber thickness [Fig. 4(b)]. Such spikes are clearly undesirable in an experimental setting, since they introduce a critical dependence of the fiber thickness on the location of the collecting plane. Depending on the height of the plane, or fluctuations of the jet, the fiber accumulation point on the collection plane corresponds to either a maximum or a minimum thickness. Moreover, one should also take into account the drying process of the fiber that could freeze the spikes into the final fiber. Thus, even though the qualitative morphological differences induced by dimensionality do not significantly affect the *time-averaged* behavior of the fiber diameter, compared to a pure horizontal driving force, the planar perturbation is not only more realistic, but also definitely more convenient from the experimental viewpoint.

We also investigate the effect of planar noise asymmetry and vertical driving force with a range of frequencies (see Figs. 5–7). A wide variety of beautiful helices is obtained in this way, confirming the richness of the phenomenology shown by the dynamics of electrified jets. We find that the planar driving force remains the best design principle. In fact, by introducing asymmetry in the planar noise, we quickly move towards the one-dimensional scenario with sharper turns that locally thicken the fiber. We also find that an additional vertical driving force does not provide a significant reduction of the fiber thickness. In the future, we plan to include an additional component of the driving force along the Z axis and/or consider an oscillating external field in the model.

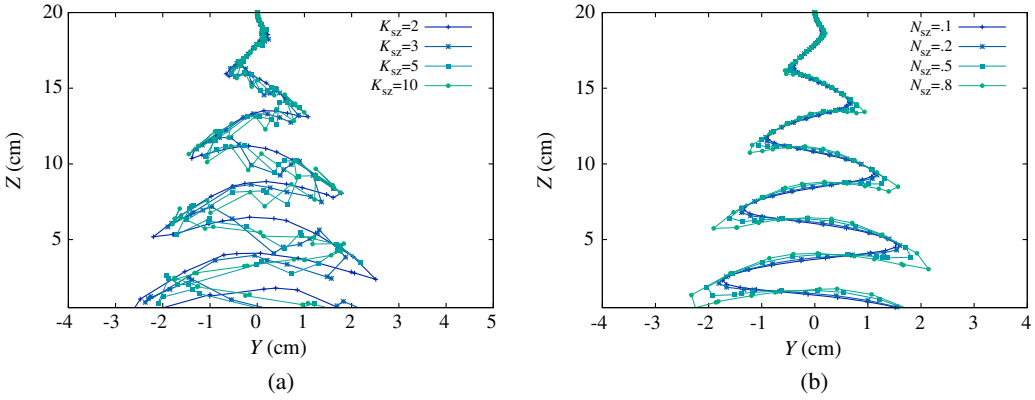

FIG. 6. Spiral jet generated under the presence of a vertical driving force along the Z axis on the pendant drop with a symmetric planar noise ($N_{\mathrm{sy}} = 1$). For clarity, we plot only the projection on the ZY plane, but it should be noted that the spirals all keep their circular symmetry on the XY plane. The parameters used for the simulations are $V_0 = 10^4$ V, $I_F = 5 \times 10^4$, and $h = 20$ cm. (a) Spiral structures for different values of the relative load frequency K_{sz} to the planar noise frequency $K_s = 5 \times 10^3$ and a fixed noise strength $N_{sz} = N_s = 10^{-3}$. (b) Jet profile plotted for a range of relative noise intensities N_{sz} with respect to the XY-plane noise $N_s = 10^{-3}$ at a fixed frequency $K_s = 5 \times 10^3$. The results indicate that even large vertical noises do not affect considerably the shape of the helix, and, in particular, they do not lead to thinner fibers.

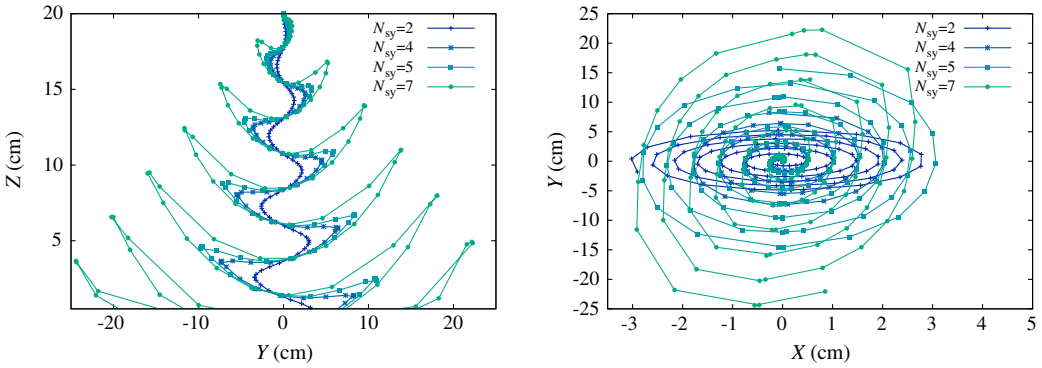

FIG. 7. Plot of the jet profile projected on the YZ plane (a) and XY plane (b) for various relative intensities N_{sy} of the noise along the Y axis with respect to the noise N_s on the XY plane. $V_0 = 10^4$ V, $I_F = 5 \times 10^4$, $N_s = 10^{-3}$, and $h = 20$ cm. The greater the asymmetry in the noise, the larger the asymmetry in the helix profile as visible in (b). Note that the scales of the X and Y axes are significantly different here. This transition is rather fast to the point that above an asymmetry ratio of $N_{sy} = 7$ we cannot get stable numerical solutions any more, and already at $N_{sy} = 7$ the helix gets deformed towards 1D banana shape profiles [Fig. 5(a)].

B. Effect of the perturbation frequency

We also explore the effect of the perturbation frequency Ω by running a series of simulations with $\Omega = 10^4, 10^5, 5 \times 10^5, 10^6$ s^{-1}, for both planar and three-dimensional scenarios. The corresponding spiral structures are shown in Figs. 8 and 9, respectively. From these figures, it is apparent that the main effect of increasing the perturbation frequency is to produce more compact and broader structures, i.e.,

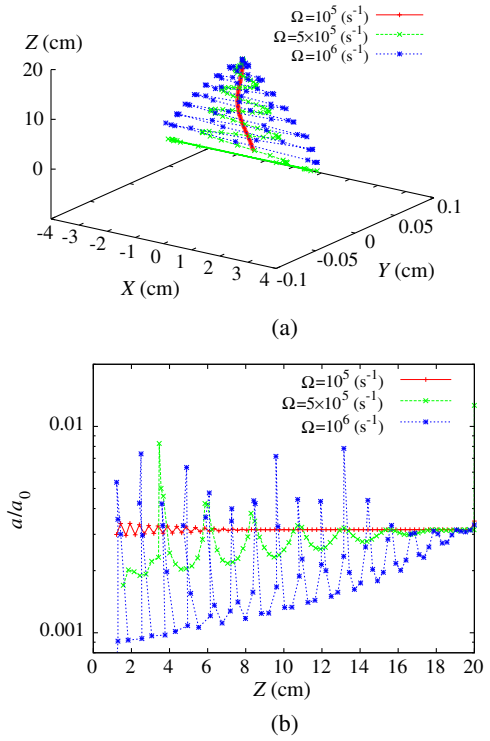

FIG. 8. (a) The spiral structures for different values of the load frequency in the one-dimensional driving scenario along the X axis. Parameters used for the simulations are $V_0 = 10^4$ V, $I_F = 5 \times 10^4$, $N_s = 10^{-3}$, and $h = 20$ cm. (b) Corresponding fiber extension plot, where the characteristic spikes due to the local bending are visible. As for the circular case, also in this case the increase in frequency results in thinner fibers.

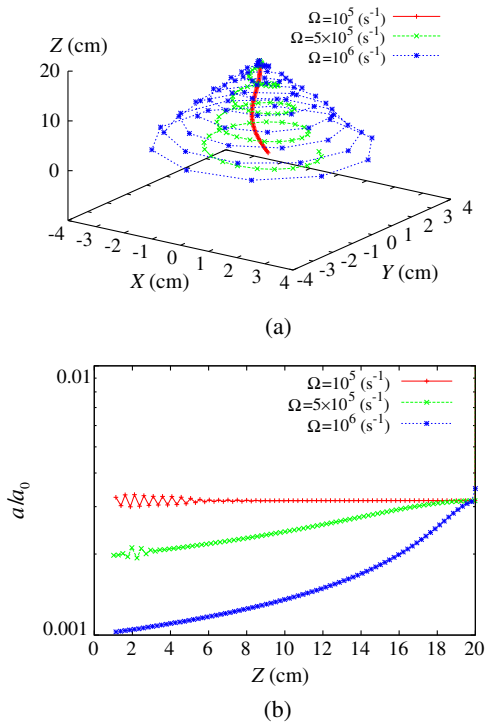

FIG. 9. Comparison of the profiles obtained with different values of the perturbation frequency Ω. Parameters used for the simulations are as above except for Ω. (a) Final configuration of the filament under a circular perturbation. (b) Plot of the elongation as a function of the distance from the collector. Similarly to what observed by varying the perturbation strength (Fig. 3), also upon increasing the frequency Ω the radius of the spirals increases and stretches the fiber.

spirals with a larger aperture and a shorter pitch. This effect can be traced back to the fact that, by increasing the perturbation frequency, the Coulomb repulsion in the XY plane is enhanced, thus leading to a larger ratio between the horizontal and vertical speeds and, hence, a shorter pitch. Thus, increasing the frequency leads again to thinner fibers at the collector, offering an additional design parameter, which minimizes the fiber thickness. To the best of our knowledge, such a design parameter has not been considered before.

C. Effect of the location of the perturbation source

In most experiments, the polymer jet is seen to fall down along a straight-line configuration, prior to the development of bending instabilities. In other words, a vertical neck precedes the formation of spiral structures. Here, we have not been able to find any parameter regime for which the neck would smoothly develop into a spiral structure: The two configurations do not appear to belong together. What we have found instead is that spirals start precisely at the location where the perturbation is applied, which means that, when the perturbation is applied at the spinneret, no neck is observed.

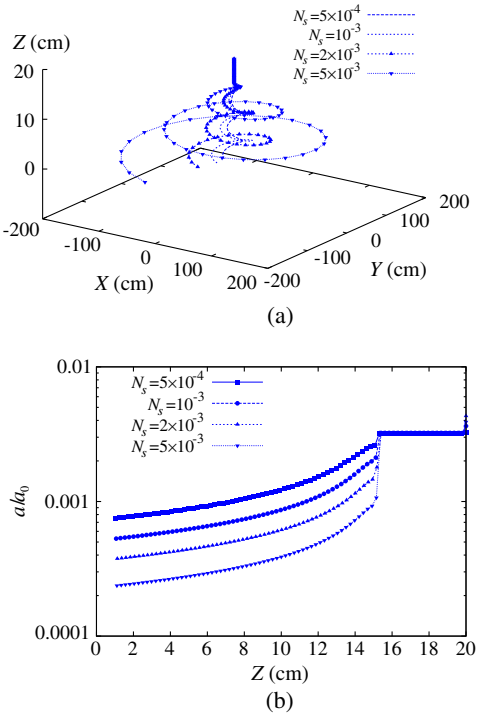

FIG. 10. Effect on the spiral shape of the mechanical load applied 5 cm below the pendant drop for various values of the load strength N_s. (a) Final configurations of the filament. Parameters are as above except for N_s. (b) Elongation as a function of the distance from the collector. Above the height of 15 cm, the location of the perturbation source, the fiber does not stretch appreciably.

To illustrate this point, in Fig. 10, we report the configuration of the spiral and the thickness of the jet, for a case where the perturbation is applied 5 cm below the pendant drop. The jet shows a clear neck, up precisely to the point where the planar perturbation is applied. Subsequently, the spiral forms in the very same way as it does when the perturbation is placed at the pendant drop. A series of simulations is carried out by changing the location of the perturbation, always to find the same result: The spiral starts to develop precisely at the perturbation location. Furthermore, we observe that, upon impinging on the collector, the jet forms planar coil patterns, similar to those observed in experiments, as one would expect for a thread falling on a stationary surface [40].

These findings suggest that the presence of the neck might reflect a different and more elaborate pathway to instability than just mechanical perturbation at the spinneret. Among others, a possibility is provided by environmental fluctuations, say, electrostatic or perhaps hydrodynamic ones, which may require a finite waiting time before building up sufficient strength to trigger bending instabilities. The importance of the formation of the neck on the development of the instability is discussed in the work of Li *et al.* [41,42], where a detailed analysis of the initial step of the spinning process is developed and linked to the physicochemical properties of the polymer solution jet. The results presented in the work of Li *et al.* suggest a strong dependence of the instability on such parameters. In the present study, we also consider a broad spectrum of different physical parameters with respect to the one that define the nondimensional quantities in Table I (results not shown). For some values of the parameters, we could not produce helices, suggesting that the properties of the polymer solutions strongly affect the instability process, hence in qualitative agreement with the results of Li *et al.* [41,42]. However, even when we do detect helices, we still cannot observe any qualitative change of the picture presented in this work, namely, that planar oscillations driving the spinneret offer a viable route to produce much thinner fibers, regardless of the chemical physical properties of the polymer solution. A detailed analysis of the effect of the solutions used in the experiments will be the object of future work.

V. CONCLUSIONS

In summary, we present a computational study of the effects of a fast-oscillating perturbation on the formation and dynamics of spiral structures in electrified jets used for electrospinning experiments. In particular, we provide numerical evidence of a direct dependence of the spiral aperture on the perturbation amplitude and frequency. As a result, our simulations suggest that both parameters could be tuned in order to minimize the fiber thickness at the collector, by maximizing the spiral length. This tuning might open up optimal design protocols in electrospinning

experiments. In other words, independently of the rheology of the polymer solution, provided that fibers can be electrospun, applying a driving perturbation oscillating at high frequency at the pendant drop can further reduce the thickness.

ACKNOWLEDGMENTS

M. Bernaschi and U. Amato are kindly acknowledged for computational help with the project. The research leading to these results has received funding from the European Research Council under the European Union's Seventh Framework Program (FP/2007-2013)/ERC Grant Agreement No. 306357 (ERC Starting Grant "NANO-JETS"). One of the authors (S. S.) acknowledges the Erwin Schroedinger Institute (ESI), for kind hospitality and financial support under the ESI Senior Fellow program.

[1] Alexander L. Yarin, *Free Liquid Jets and Films: Hydrodynamics and Rheology* (Longman, New York, 1993).
[2] Darrell H. Reneker, Alexander L. Yarin, Hao Fong, and Sureeporn Koombhongse, Bending instability of electrically charged liquid jets of polymer solutions in electrospinning, J. Appl. Phys. **87**, 4531 (2000).
[3] A. L. Yarin, S. Koombhongse, and D. H. Reneker, Taylor cone and jetting from liquid droplets in electrospinning of nanofibers, J. Appl. Phys. **90**, 4836 (2001).
[4] I. G. Loscertales, A. Barrero, I. Guerrero, R. Cortijo, M. Marquez, and A. M. Gañán Calvo, Micro/nano encapsulation via electrified coaxial liquid jets, Science **295**, 1695 (2002).
[5] Yuris A. Dzenis, Spinning continuous fibers for nanotechnology, Science **304**, 1917 (2004).
[6] Matthew E. Helgeson, Kristie N. Grammatikos, Joseph M. Deitzel, and Norman J. Wagner, Theory and kinematic measurements of the mechanics of stable electrospun polymer jets, Polymer **49**, 2924 (2008).
[7] C. J. Thompson, G. G. Chase, A. L. Yarin, and D. H. Reneker, Effects of parameters on nanofiber diameter determined from electrospinning model, Polymer **48**, 6913 (2007).
[8] Dirk Grafahrend, Karl-Heinz Heffels, Meike V. Beer, Peter Gasteier, Martin Möller, Gabriele Boehm, Paul D. Dalton, and Jürgen Groll, Degradable polyester scaffolds with controlled surface chemistry combining minimal protein adsorption with specific bioactivation, Nat. Mater. **10**, 67 (2011).
[9] Israel Greenfeld, Kamel Fezzaa, Miriam H. Rafailovich, and Eyal Zussman, Fast x-ray phase-contrast imaging of electrospinning polymer jets: Measurements of radius, velocity, and concentration, Macromolecules **45**, 3616 (2012).
[10] M. Serdar Onses, Chiho Song, Lance Williamson, Erick Sutanto, Placid M. Ferreira, Andrew G. Alleyne, Paul F. Nealey, Heejoon Ahn, and John A. Rogers, Hierarchical patterns of three-dimensional block-copolymer films formed by electrohydrodynamic jet printing and self-assembly, Nat. Nanotechnol. **8**, 667 (2013).
[11] Sung-Yong Min, Tae-Sik Kim, Beom Joon Kim, Himchan Cho, Yong-Young Noh, Hoichang Yang, Jeong Ho Cho, and Tae-Woo Lee, Large-scale organic nanowire lithography and electronics, Nat. Commun. **4**, 1773 (2013).
[12] Omri Regev, Arkadii Arinstein, and Eyal Zussman, Creep anomaly in electrospun fibers made of globular proteins, Phys. Rev. E **88**, 062605 (2013).
[13] Atsushi Nakano, Norihisa Miki, Koichi Hishida, and Atsushi Hotta, Solution parameters for the fabrication of thinner silicone fibers by electrospinning, Phys. Rev. E **86**, 011801 (2012).
[14] Andreas Greiner and Joachim H Wendorff, Electrospinning: A fascinating method for the preparation of ultrathin fibers, Angew. Chem., Int. Ed. Engl. **46**, 5670 (2007).
[15] Sergey V. Fridrikh, Jian H. Yu, Michael P. Brenner, and Gregory C. Rutledge, Controlling the fiber diameter during electrospinning, Phys. Rev. Lett. **90**, 144502 (2003).
[16] Andrea Camposeo, Luana Persano, and Dario Pisignano, Light-emitting electrospun nanofibers for nanophotonics and optoelectronics, Macromol. Mater. Eng. **298**, 487 (2013).
[17] Dario Pisignano, *Polymer Nanofibers: Building Blocks for Nanotechnology* (Royal Society of Chemistry, Cambridge, England, 2013), p. 29.
[18] G. Taylor, Electrically driven jets, Proc. R. Soc. A **313**, 453 (1969).
[19] Alvaro G. Marin, Guillaume Riboux, Ignacio G. Loscertales, and Antonio Barrero, Whipping instabilities in electrified liquid jets, arXiv:0810.0155.
[20] Haiqing Liu, Christian H. Reccius, and H. G. Craighead, Single electrospun regioregular poly(3-hexylthiophene) nanofiber field-effect transistor, Appl. Phys. Lett. **87**, 253106 (2005).
[21] Luana Persano, Andrea Camposeo, Pompilio Del Carro, Vito Fasano, Maria Moffa, Rita Manco, Stefania D'Agostino, and Dario Pisignano, Lasers: Distributed feedback imprinted electrospun fiber lasers, Adv. Mater. **26**, 6542 (2014).
[22] José M. Moran-Mirabal, Jason D. Slinker, John A. DeFranco, Scott S. Verbridge, Rob Ilic, Samuel Flores-Torres, Héctor Abruña, George G. Malliaras, and H. G. Craighead, Electrospun light-emitting nanofibers, Nano Lett. **7**, 458 (2007).
[23] Varun Vohra, Umberto Giovanella, Riccardo Tubino, Hideyuki Murata, and Chiara Botta, Electroluminescence from conjugated polymer electrospun nanofibers in solution processable organic light-emitting diodes, ACS Nano **5**, 5572 (2011).
[24] Meghana V. Kakade, Steven Givens, Kenncorwin Gardner, Keun Hyung Lee, D. Bruce Chase, and John F. Rabolt, Electric field induced orientation of polymer chains in macroscopically aligned electrospun polymer nanofibers, J. Am. Chem. Soc. **129**, 2777 (2007).
[25] Stefano Pagliara, Miriam S. Vitiello, Andrea Camposeo, Alessandro Polini, Roberto Cingolani, Gaetano Scamarcio, and Dario Pisignano, Optical anisotropy in single light-emitting polymer nanofibers, J. Phys. Chem. C **115**, 20399 (2011).
[26] Marie Richard-Lacroix and Christian Pellerin, Orientation and structure of single electrospun nanofibers of

poly(ethylene terephthalate) by confocal Raman spectroscopy, Macromolecules **45**, 1946 (2012).

[27] Stefano Pagliara, Andrea Camposeo, Alessandro Polini, Roberto Cingolani, and Dario Pisignano, Electrospun light-emitting nanofibers as excitation source in microfluidic devices, Lab Chip **9**, 2851 (2009).

[28] Jingwei Xie, Matthew R. MacEwan, Xiaoran Li, Shelly E. Sakiyama-Elbert, and Younan Xia, Neurite outgrowth on nanofiber scaffolds with different orders, structures, and surface properties, ACS Nano **3**, 1151 (2009).

[29] Arkadii Arinstein, Michael Burman, Oleg Gendelman, and Eyal Zussman, Effect of supramolecular structure on polymer nanofiber elasticity, Nat. Nanotechnol. **2**, 59 (2007).

[30] Moses M. Hohman, Michael Shin, Gregory Rutledge, and Michael P. Brenner, Electrospinning and electrically forced jets. I. Stability theory, Phys. Fluids **13**, 2201 (2001).

[31] Moses M. Hohman, Michael Shin, Gregory Rutledge, and Michael P. Brenner, Electrospinning and electrically forced jets. II. Applications, Phys. Fluids **13**, 2221 (2001).

[32] Israel Greenfeld, Arkadii Arinstein, Kamel Fezzaa, Miriam H. Rafailovich, and Eyal Zussman, Polymer dynamics in semidilute solution during electrospinning: A simple model and experimental observations, Phys. Rev. E **84**, 041806 (2011).

[33] Giuseppe Pontrelli, Daniele Gentili, Ivan Coluzza, Dario Pisignano, and Sauro Succi, Effects of non-linear rheology on electrospinning process: A model study, Mech. Res. Commun. **61**, 41 (2014).

[34] Daoheng Sun, Chieh Chang, Sha Li, and Liwei Lin, Near-field electrospinning, Nano Lett. **6**, 839 (2006).

[35] Gobind S. Bisht, Giulia Canton, Alireza Mirsepassi, Lawrence Kulinsky, Seajin Oh, Derek Dunn-Rankin, and Marc J. Madou, Controlled continuous patterning of polymeric nanofibers on three-dimensional substrates using low-voltage near-field electrospinning, Nano Lett. **11**, 1831 (2011).

[36] Chia-Ling Pai, Mary C. Boyce, and Gregory C. Rutledge, Mechanical properties of individual electrospun PA 6(3)T fibers and their variation with fiber diameter, Polymer **52**, 2295 (2011).

[37] Alexander L. Yarin, Strong flows of polymeric liquids, J. Non-Newtonian Fluid Mech. **37**, 113 (1990).

[38] Darrell H. Reneker and Alexander L. Yarin, Electrospinning jets and polymer nanofibers, Polymer **49**, 2387 (2008).

[39] P. K. Bhattacharjee and G. C. Rutledge, in *Comprehensive Biomaterials*, edited by P. Ducheyne, K. E. Healy, D. W. Hutmacher, D. W. Grainger, and C. J. Kirkpatrick (Elsevier, Oxford, 2011).

[40] S. Chiu-Webster and J. R. Lister, The fall of a viscous thread onto a moving surface: A fluid-mechanical sewing machine, J. Fluid Mech. **569**, 89 (2006).

[41] Fang Li, Alfonso M. Gañán Calvo, José M. López-Herrera, Xie-Yuan Yin, and Xie-Zhen Yin, Absolute and convective instability of a charged viscoelastic liquid jet, J. Non-Newtonian Fluid Mech. **196**, 58 (2013).

[42] Fang Li, Xie-Yuan Yin, and Xie-Zhen Yin, Instability analysis of a coaxial jet under a radial electric field in the nonequipotential case, Phys. Fluids **18**, 037101 (2006).